Chemical Engineering Journal 456 (2023) 140956

Contents lists available at ScienceDirect

Chemical Engineering Journal

journal homepage: www.elsevier.com/locate/cej

In situ laser-assisted synthesis and patterning of graphene foam composites as a flexible gas sensing platform

Jiang Zhao [a,1], Ning Yi [b,d,1], Xiaohong Ding [a], Shangbin Liu [a], Jia Zhu [a,e], Alexander C. Castonguay [c], Yuyan Gao [a], Lauren D. Zarzar [b,c,d], Huanyu Cheng [a,b,d,*]

[a] Department of Engineering Science and Mechanics, The Pennsylvania State University, University Park, PA 16802, USA
[b] Department of Materials Science and Engineering, The Pennsylvania State University, University Park, PA 16802, USA
[c] Department of Chemistry, The Pennsylvania State University, University Park, PA 16802, USA
[d] Materials Research Institute, The Pennsylvania State University, University Park, PA 16802, USA
[e] School of Materials and Energy, University of Electronic Science and Technology of China, Chengdu 610054, China

ARTICLE INFO

Keywords:
Laser-induced graphene foam composites
Metal oxides
Molybdenum disulfide
Stretchable gas sensing platform

ABSTRACT

Gas-sensitive semiconducting nanomaterials (e.g., metal oxides, graphene oxides, and transition metal dichalcogenides) and their heterojunctions hold great promise in chemiresistive gas sensors. However, they often require a separate synthesis method (e.g., hydrothermal, so-gel, and co-precipitation) and their integration on interdigitated electrodes (IDE) via casting is also associated with weak interfacial properties. This work demonstrates in situ laser-assisted synthesis and patterning of various sensing nanomaterials and their heterojunctions on laser-induced graphene (LIG) foam to form LIG composites as a flexible and stretchable gas sensing platform. The porous LIG line or pattern with nanomaterial precursors dispensed on top is scribed by laser to allow for in situ growth of corresponding nanomaterials. The versatility of the proposed method is highlighted through the creation of different types of gas-sensitive materials, including transition metal dichalcogenide (e.g., MoS_2), metal oxide (e.g., CuO), noble metal-doped metal oxide (e.g., Ag/ZnO) and composite metal oxides (e.g., In_2O_3/Cr_2O_3). By eliminating the IDE and separate heaters, the LIG gas sensing platform with self-heating also decreases the device complexity. The limit of detection (LOD) of the LIG gas sensor with in situ synthesized MoS_2, CuO, and Ag/ZnO to NO_2, H_2S, and trimethylamine (TMA) is 2.7, 9.8, and 5.6 ppb, respectively. Taken together with the high sensitivity, good selectivity, rapid response/recovery, and tunable operating temperature, the integrated LIG gas sensor array can identify multiple gas species in the environment or exhaled breath.

1. Introduction

The critical role of flexible and stretchable gas sensors in the revolution of the smart internet of things provides unique application opportunities in industrial safety [1], pollution monitoring [2], and personal healthcare [3]. The laser-induced graphene (LIG) foam with a 3D microporous structure can be simply fabricated by laser scribing of commercial polyimide film (Kapton) or other carbon-containing materials in ambient conditions to create a stretchable gas sensing platform [4–6]. The high specific surface area, excellent gas permeability, and low-cost fabrication process of the LIG result in gas sensors with superior performance parameters. Besides intrinsic LIG to detect O_2, N_2, and CO_2 with a parts-*per*-million (ppm) sensitivity [7], its integration with semiconducting nanomaterials such as metal oxide, transition metal dichalcogenides, and their noble metal doped composites can form heterojunctions for improved performance. For instance, combining LIG with MoS_2@reduced graphene oxide (MoS_2@rGO) [8], Pd nanoparticles (Pd NPs) [9], and polyvinylidene fluoride / 1-ethyl-3-methylimidazolium bis (trifluoromethylsulfonyl)-imide /Pd NPs (PVDF/ImTFSI/Pd NPs) [10] allows the sensitive detection of NO_2, H_2, and CH_4, respectively. Opportunities also exist to integrate LIG with other metal oxides, including NiO, CuO, SnO_2, TiO_3, WO_3, ZnO, Fe_2O_3, and Al_2O_3 for detecting combustible, hazardous, or toxic gas species [11]. The potential integration with transition metal dichalcogenides may include MoS_2, $MoSe_2$, WS_2, and WSe_2 (especially their 2D forms) [12,13]. Doping semiconducting gas-sensitive nanomaterials with a catalytic

* Corresponding author at: Department of Engineering Science and Mechanics, The Pennsylvania State University, University Park, PA 16802, USA.
E-mail address: huanyu.cheng@psu.edu (H. Cheng).
[1] These authors contributed equally.

https://doi.org/10.1016/j.cej.2022.140956
Received 12 October 2022; Received in revised form 6 December 2022; Accepted 11 December 2022
Available online 19 December 2022

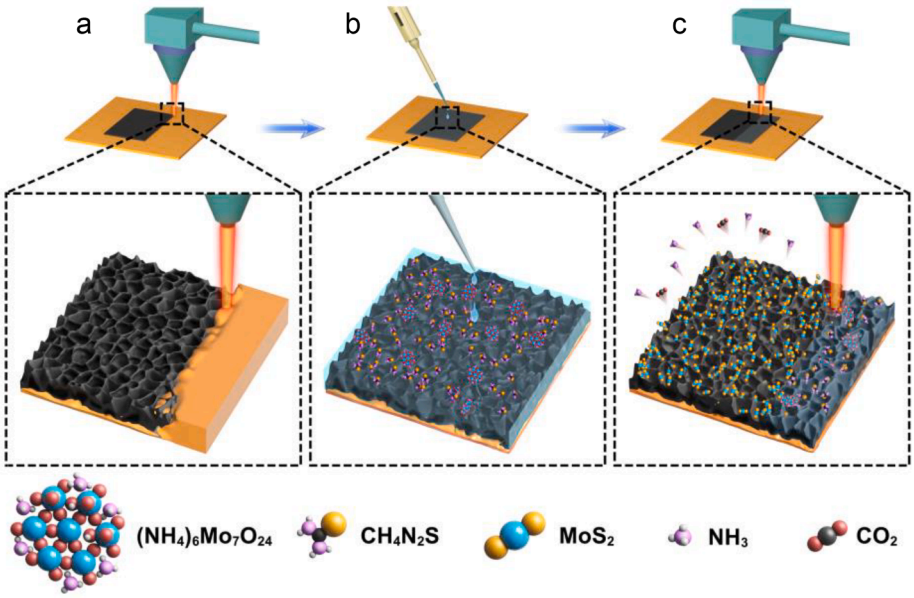

Fig. 1. Schematic showing the process of in situ growth of MoS_2 on laser-induced graphene (LIG). (a) After laser scribing to form LIG on polyimide film, (b) drop-casting and drying of precursor solution on LIG are (c) followed by another laser scribing for in situ growth of MoS_2 under an ambient environment.

noble metal such as Pd, Pt, Au, and Ag can further reduce their activation energy, increase the sensitivity, accelerate the redox reaction, and improve the response/recovery time [14,15].

The synthesis of these semiconductor gas-sensitive nanomaterials can be broadly classified into physical or chemical methods. Common physical methods include sputtering [16,17], electron-beam evaporation [18], ball milling [19], laser-assisted synthesis [20], and electrospraying [21]. Common chemical methods are sol–gel [22], hydrothermal [23], co-precipitation [24], chemical vapor deposition [25], and microemulsion [26]. However, these methods are each associated with limitations. Sputtering, electron-beam evaporation, and chemical vapor deposition require a high vacuum environment and expensive equipment. Ball-milling and hydrothermal/co-precipitation methods need a prolonged synthesis time at high temperatures and pressures. An additional calcination process at high temperature is also required for sol–gel and electrospraying. In contrast, laser ablation in liquid (LAL) and laser fragmentation in liquid (LFL) as the most widely studied laser-assisted synthesis (LAS) methods are capable of producing high-purity semiconducting nanomaterials in aqueous solution without the use of surfactants at ambient environment [27]. Besides a rich library of various types of semiconducting materials (e.g., Fe_2O_3 [28], Ag_2O [29], CoO [30], Fe-Cu oxide [31], ZnO [32], Au/WO_3 [20], and CuO[33]), these nanomaterials also exhibit different morphologies such as core–shell, dendrites, spindles, nanoflakes, and nanoflowers [34]. However, the nanomaterials dispersed in liquid require additional integration steps (e.g., dip-coating or drop-casting) and annealing steps (to increase binding stability). Various methods have also been reported to prepare flexible LIG composites, including dip-coating or drop-casting nanomaterial dispersions on LIG [8,10,35], physical or chemical vapor deposited nanomaterials on LIG [9], and laser scribing of polyimide (PI) pretreated with nanomaterial dispersants and surfactants [36] or metal-complex-containing PI films [37]. However, in situ synthesis of gas-sensitive LIG nanocomposites with robust interface from low-cost manufacturing methods has yet to be reported.

Here we report a novel in situ laser-assisted synthesis and patterning of LIG foam composites as a flexible and stretchable gas sensing platform (Fig. S1), which are rapid, surfactant-free, and processable in the ambient environment. The versatility of the method is demonstrated by in situ growth, patterning, and integration of varying gas-sensitive nanomaterials such as transition metal dihalogens (MoS_2), metal oxides (CuO), noble metal doped metal oxides (Ag/ZnO), and composite metal oxides (In_2O_3/Cr_2O_3) on LIG in a single step. The LIG composites with MoS_2, CuO, and Ag/ZnO exhibit high selectivity and low limit of detection (LOD) to detect NO_2, H_2S, and trimethylamine (TMA), respectively. The resulting gas sensing platform based on LIG composites with self-heating capability also eliminates the need for interdigitated electrodes and the separate heater to exhibit high sensitivity and rapid response/recovery. The low-cost, scalable fabrication approach can easily integrate multiple gas sensors in a large-density array as an electronic nose to potentially deconvolute multiple gas species in a mixture. Stretchable gas sensors were obtained by transferring the LIG patterns onto a soft elastomeric substrate in our previously reported work [16,17] and this paper focuses on laser-assisted synthesis of LIG composites and their different sensing properties. Taken together with other LIG-based sensing modalities (e.g., electrochemical sweat sensors [38], electrophysiological sensors [39], among others), the gas sensing platform based on the LIG composites can open up opportunities for the next-generation soft, deformable devices for healthcare.

2. Experimental section

2.1. Materials

Zinc nitrate hexahydrate ($Zn(NO_3)_2{\cdot}6H_2O$), silver nitrate ($AgNO_3$), ammonium paramolybdate ($(NH_4)_6Mo_7O_{24}$), sodium molybdate dihydrate ($Na_2MoO_4{\cdot}2H_2O$), thiourea (CH_4N_2S), copper(II) nitrate trihydrate ($Cu(NO_3)_2{\cdot}3H_2O$) were obtained from Sigma-Aldrich and used as received without further purification. Silver nitrate saturated solution was prepared by dissolving 55 g $AgNO_3$ in 20 mL deionized (DI) water. PI tape (Kapton 3 M, 170 μm thickness) was purchased from CS Hyde.

2.2. Characterizations

XRD was conducted using a Rigaku Ultima IV with a Cu target. Raman spectroscopy was performed by a HORIBA Scientific LabRAM HR Evolution with a laser excitation wavelength of 532 nm for Mo-S-LIG-w, 633 nm for Cu-LIG-w, and 514 nm for Ag-Zn-LIG-w and In-Cr-LIG-w. SEM images were obtained using a TESCAN VEGA3. All samples were characterized on PI films.

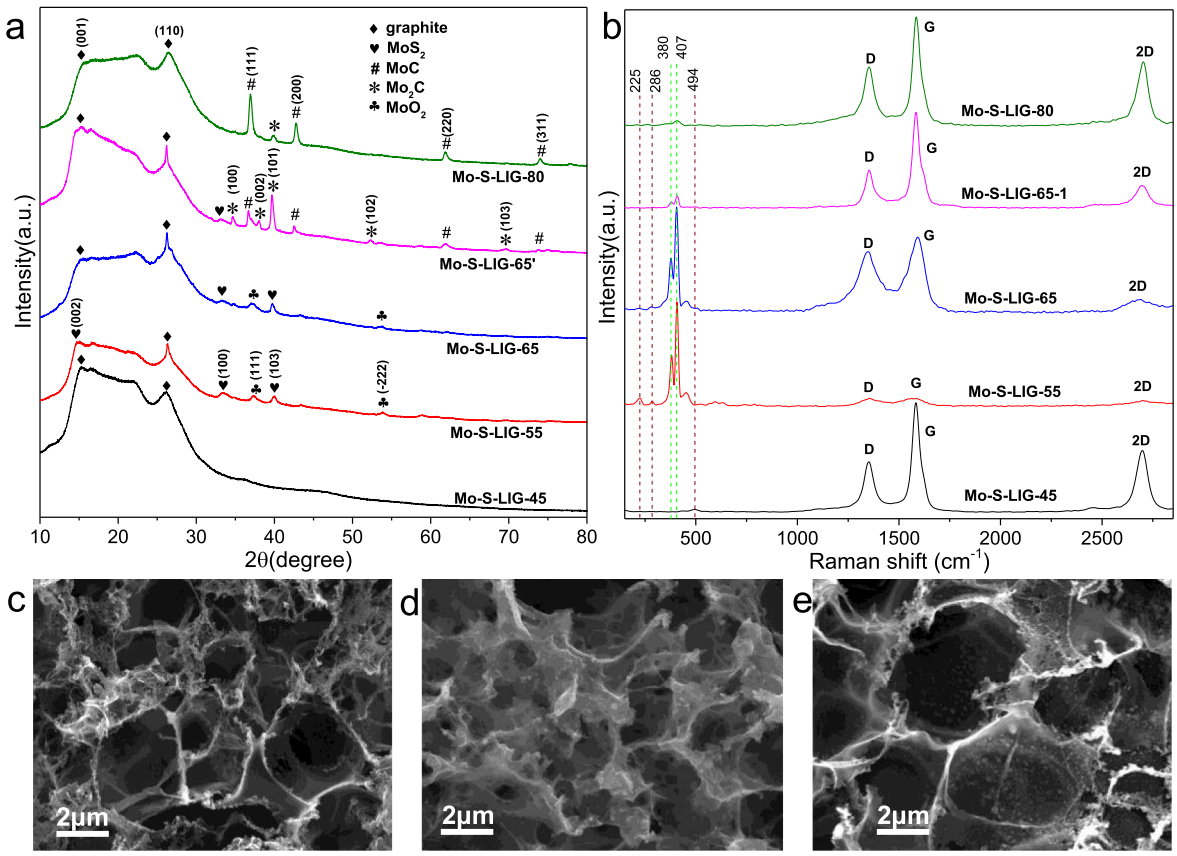

Fig. 2. Structure characterizations of Mo-S-LIG-w with w for the power percentage ratio of the second laser scribing power to the initially used. (a) XRD and (b) Raman spectra of Mo-S-LIG-w (note: Mo-S-LIG-65′ was scribed at an image density of 6 and the others were of 4). SEM of (c) bare LIG, (d) Mo-S-LIG-55, (e) Mo-S-LIG-65.

2.3. Gas sensor testing

A sourcemeter (Keithley 2400) was used for all measurements and data acquisition. Due to the Joule heating effect, the measurement voltage applied by the sourcemeter simultaneously increased the temperature of the LIG single line. The output voltage was set according to the LIG line's temperature measured by the thermal imaging camera (FLIR ONE PRO). The gas sensor was placed in a sealed gas chamber filled with target gas species of a specific concentration and the resistance of the sensor was continuously measured during testing. The sensor response was calculated using $\Delta R/R_0$, where R_0 is the resistance in air and ΔR is the resistance change in target gas from the air.

3. Results and discussion

3.1. In situ growth of transition metal dichalcogenide and metal oxide on LIG

The in situ growth of MoS_2 (or metal oxides) on LIG starts with scribing a thin polyimide film (thickness of 170 μm) with a CO_2 laser (power of 18 %, speed of 7 %) to form LIG (Fig. 1a). The surface wettability of LIG is related to the atmosphere during laser scribing[40]. Using ambient air rather than inert or reducing gas results in LIG with a superhydrophilic top surface, which facilitates the dispersion of the precursor solution. After rinsing the fabricated LIG with deionized water and then ethanol, drop-casting and drying of the precursor solution on the LIG (Fig. 1b) are followed by another laser scribing process at different powers (Fig. 1c). Rinsing the final film with deionized water and ethanol again removes residual reactants. The aqueous MoS_2 precursor solution consists of 0.07 M ammonium paramolybdate and 3 M thiourea. Similarly, the aqueous CuO, Ag/ZnO, and In_2O_3/Cr_2O_3 precursor solutions are prepared with 0.5 M copper nitrate, a mixture of 0.03 M silver nitrate and 0.5 M zinc nitrate, and a mixture of 0.5 M indium nitrate and 0.5 M chromium nitrate, respectively. The resulting samples are denoted as M−LIG−w, where M represents the element of the transition metal dichalcogenide or metal oxide (e.g., Mo-S, Cu, Ag-Zn, In-Cr) and w represents the power percentage ratio of the second laser scribing power to the initially used.

3.2. Structural and morphological studies

Characterization of the as-prepared LIG composites involves the use of X-ray diffraction (XRD), Raman spectroscopy, and scanning electron microscopy (SEM). The diffraction peaks at 2Θ of 14.9° and 25.8° in the XRD correspond to (0 0 1) and (1 1 0) planes of orthorhombic graphite (JCPDS No. 89–8489), respectively (Fig. 2a and S2a). Taken together with large envelopes in all samples, these results indicate the formation of low crystallinity graphite. For a proper laser power (i.e., 55 %~65 % of the initial power for the second scribing), the locally heating on LIG decomposite ammonium paramolybdate and react with thiourea to form MoS_2, as evidenced by characteristic peaks of the (0 0 2), (1 0 0), (1 0 3) planes of hexahedral MoS_2 and (1 1 1), (–2 2 2) planes of monoclinic MoO_2. Further increasing the laser power (Mo-S-LIG-80) or the image density (Mo-S-LIG-65′) results in the formation of Mo_2C (characteristic peaks of the (1 0 0), (0 0 2), (1 0 2), and (1 0 3) planes of hexagonal Mo_2C) and MoC (characteristic peaks of the (1 1 1), (2 0 0), (2 2 0), and (3 1 1) planes of cubic MoC). This result comes from the reaction of MoS_2 with carbon in LIG under a stronger localized thermal effect. On the other hand, the above characteristic peaks are not observed when the power percentage ratio (w) of the second laser scribing power to the initially

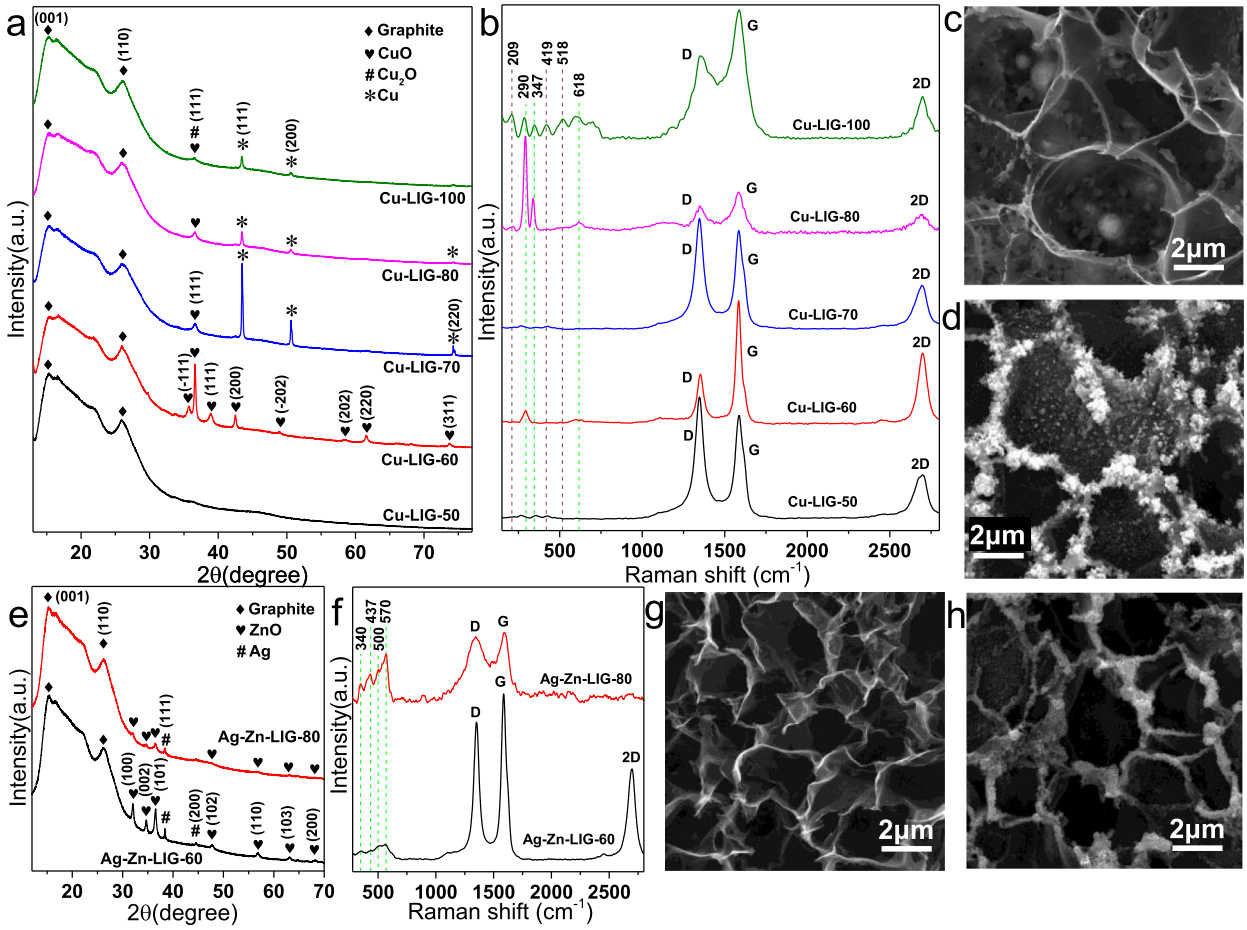

Fig. 3. Structural characterizations of Cu-LIG-w and Ag-Zn-LIG-w. (a) XRD and (b) Raman spectra of Cu-LIG-w. SEM images of (c) Cu-LIG-60 and (d) Cu-LIG-80. (e) XRD spectra, (f) Raman spectra, and SEM of (g) Ag-Zn-LIG-60 and (h) Ag-Zn-LIG-80.

used is 45 %, indicating the unsuccessful growth of the Mo-based compound. Therefore, laser power is a key parameter to modulate the composition of the synthesized LIG composites.

The structural characterization of the Mo-S-LIG-w with Raman reveals the D Peak at ~ 1,350 cm^{-1}, G Peak at ~ 1,585 cm^{-1}, and 2D peak at ~ 2,700 cm^{-1} in all 5 samples to confirm the generation of the LIG (Fig. 2b and S2b). In the Raman of the Mo-S-LIG-55, E_{2g} and A_{1g} vibration modes of strong MoS_2 peaks appear at 380 cm^{-1} and 407 cm^{-1}, respectively as in previously reported studies [41,42] (with weak peaks at 225 cm^{-1} and 286 cm^{-1} from MoO_2) [43,44]. Meanwhile, the Mo-S-LIG-55 has the weakest graphene peaks of all the samples, which is attributed to the formation and covering of amorphous MoS_2 on the porous surface of LIG (Fig. 2c-d) to decrease Raman scattering of graphene. The reduced coverage of amorphous MoS_2 on the LIG in Mo-S-LIG-65 (Fig. 2e) shows strong peaks of graphene. Furthermore, the decreased MoS_2 peaks in Mo-S-LIG-65′ scribed at a larger image density verifies the decomposition of MoS_2 caused by the higher degree of laser spot overlapping. Only the weak peak at 407 cm^{-1} among the peaks attributed to MoS_2 can be seen in Mo-S-LIG-80 verifies the reaction of MoS_2 with carbon at high temperature. The results of Raman and SEM are consistent with XRD analysis. The EDS images also confirm the uniform distribution of MoS_2 in the LIG region (Fig. S3a).

The XRD of the Cu-LIG-w in all 5 samples (scribed at image density 6) shows envelopes and the (0 0 1) and (1 1 0) planes of graphite (JCPDS No. 89–8489) (Fig. 3a). The Cu-LIG-60 exhibits the characteristic (1 1 1), (2 0 0), (2 2 0), (3 1 1) planes of cubic CuO (JCPDS No. 78–0428) and the characteristic (−1 1 1), (1 1 1), (−2 0 2), (2 0 2) planes of monoclinic CuO (JCPDS No. 89–5896). As the power percentage ratio is increased from 60 to 70 % in the Cu-LIG-70, the (1 1 1) plane of cubic CuO can be seen to show up with the characteristic (1 1 1), (2 0 0), and (2 2 0) planes of Cu (JCPDS card number 70–3039). The presence of Cu is because part of CuO is reduced by carbon with an increased laser thermal effect. However, a further increase in the power percentage ratio to 80 and 100 % shows decreased sharp Cu peaks in Cu-LIG-80 and Cu-LIG-100 due to simultaneous oxidation of Cu. The above analysis is confirmed by the Raman spectroscopy (Fig. 3b). As the power percentage ratio is increased from 60 to 70 %, the Ag mode of CuO with a weak peak at 290 cm^{-1} in Cu-LIG-60 disappears in Cu-LIG-70 due to the reduction of CuO. It should be noted that Cu cannot be observed either because the metal has no Raman activity. Cu-LIG-80 shows two strong peaks at 290 cm^{-1} and 347 cm^{-1} and one weak peak at 618 cm^{-1}, corresponding to A_g, B_{1g}, and B_{2g} modes of CuO, respectively [45,46]. Besides these three peaks of CuO, peaks at 209 cm^{-1}, 419 cm^{-1} and 518 cm^{-1} can also be seen in Cu-LIG-100, which are from the second-order Raman-allowed mode ($2\Gamma_{12}$), fourth-phonon mode ($4\Gamma_{12}$) and the Raman-allowed mode (Γ_{25}) of Cu_2O, respectively [47,48]. These additional peaks from Cu_2O confirm partial decomposition of CuO to Cu_2O under a stronger thermal effect. Taken together with the fact of no other diffraction peaks from CuO and Cu_2O (but only the weak and broadened (1 1 1) plane) in the XRD patterns of Cu-LIG-80 and Cu-LIG-100, the generated CuO and Cu_2O are mostly amorphous. The SEM image of Cu-LIG-60 shows thin walls of LIG with spherules in the holes of the porous structure (Fig. 3c) to indicate an incomplete reaction from lower laser power. In contrast, a large number of CuO particles are generated and aggregated on the walls of the porous LIG in Cu-LIG-80 (Fig. 3d).

The XRD of Ag-Zn-LIG-60 and Ag-Zn-LIG-80 exhibits characteristic

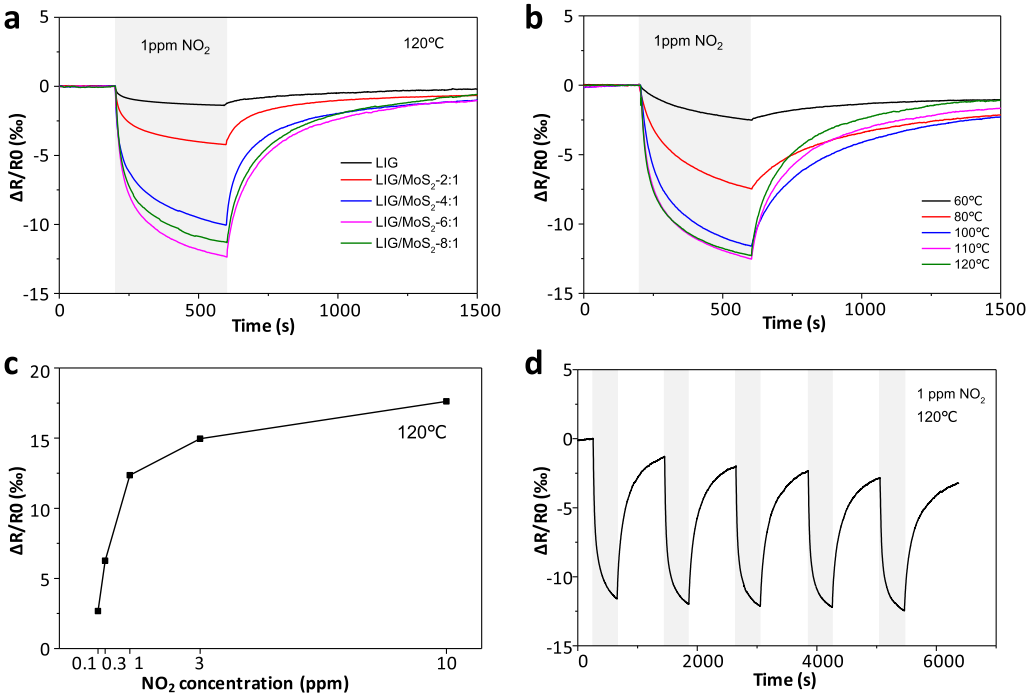

Fig. 4. The gas-sensing performance of LIG/MoS_2 to NO_2. (a) The response of LIG/MoS_2 gas sensor fabricated with precursor solutions of various concentrations to 1 ppm NO_2 at 120 °C (the bare LIG sensor used as a reference). (b) The effect of operating temperature on the response of LIG/MoS_2-6:1 to 1 ppm NO_2. (c) The sensitivity of LIG/MoS_2-6:1 to various NO_2 concentrations at 120 °C. (d) The cycling test of LIG/MoS_2-6:1 to 1 ppm NO_2.

(100), (002), (101), (102), (110), (103), and (200) planes of ZnO (JCPDS No. 89–7102) in both samples (Fig. 3e). Because Ag^+ is more oxidizing than Zn^{2+}, Ag^+ is reduced to Ag by carbon to show the (111) and (200) planes of Ag (JCPDS No. 87–0720). Stronger localized thermal effect leads to the higher amount of generated ZnO in Ag-Zn-LIG-80, with peaks at 340 cm^{-1}, 437 cm^{-1}, and 570 cm^{-1} corresponding to 2E2 (M), E2 (high) and A1 (LO) modes [49,50] (Fig. 3f). The peak at 500 cm^{-1} corresponds to the local vibrational mode (LVM) induced by the Ag dopant [51]. Due to the low yield of ZnO at the lower power, no obvious particles can be seen in the SEM image of the Ag-Zn-LIG-60 (Fig. 3g). In contrast, more amorphous materials can be seen to aggregate on the wall of the porous LIG structure in Ag-Zn-LIG-80 due to increased power (Fig. 3h), which agrees well with the results of XRD (lower peak intensity due to the coverage of amorphous ZnO) and Raman. Additionally, the successful growth of In_2O_3 and Cr_2O_3 on the LIG can be confirmed by the XRD, Raman, and SEM images of In-Cr-LIG-80 (Fig. S4). The uniform distributions of CuO, ZnO, In_2O_3, and Cr_2O_3 in the LIG region are confirmed by EDS mapping (Fig. S3b-d).

Most of the metal nitrates are soluble in water and decompose into metal oxides, oxygen and nitrogen dioxides when heated, making them an excellent choice as precursors in this work. While it is possible to explore the other precursors such as metal chlorides, it is much more complicated. For instance, replacing zinc nitrate with zinc chloride solution and processing with the same laser parameters do not give zinc oxide crystals (Fig.S5). The methods using other kinds of salts as precursors will be explored in future studies.

3.3. Fabrication of gas sensors

After elucidating the relationship between the laser processing parameters and structures of the LIG composites, their further relationship with the gas sensing performance is investigated. The LIG pattern designed in a dumbbell shape with a single line as the sensing region allows the modulation of the temperature upon an externally applied voltage (and two contact pads for connecting to the sourcemeter) due to the Joule heating effect [7]. The simple fabrication process can easily yield a gas sensor array based on LIG composites (with MoS_2, CuO, or Ag/ZnO) for the deconvolution of multiple species in a mixture (Fig. S6). In brief, after creating the single line with a line width of 240 μm and a length of 2.5 mm in the bare LIG patterns with laser scribing (Fig. S6a), drop-casting the precursor solution (4 μL) on the single line region is followed by another lased scribing (Fig. S6b-c). The MoS_2 precursor solution (denoted as MoS_2-m) with varying S^{2-}/Mo^{6+} molar ratios m (i.e., m = 2:1, 4:1, 6:1, and 8:1, respectively) is prepared by dissolving thiourea (76 mg, 152 mg, 228 mg, and 304 mg) and ammonium paramolybdate (88 mg) in deionized (DI) water (10 mL). Similarly, the CuO precursor solution (CuO-c) with different copper nitrate concentrations c (i.e., c = 0.1 M, 0.2 M, 0.4 M, and 0.6 M, respectively) is obtained by dissolving copper nitrate (187.56 mg, 375.12 mg, 750.24 mg, and 1125.36 mg) in DI water (10 mL). The ZnO precursor solution (ZnO-0.1 M) with a zinc nitrate concentration of 0.1 M is produced by dissolving zinc nitrate hexahydrate (297.5 mg) in DI water (10 mL). Lastly, the Ag/ZnO precursor solution (Ag/ZnO-m) with an $AgNO_3/Zn(NO_3)_{2\,M}$ ratio m of 3:100, 6:100, and 9:100 is prepared by adding standard silver nitrate solution with various volumes (2.3 μL, 4.7 μL, and 7 μL) into the 0.1 M zinc nitrate solution. The laser with a power percentage ratio of 65 % (or 80 %) and an image density of 4 (or 6) is used for creating the LIG/MoS_2 (or LIG/CuO and LIG/Ag/ZnO) composite. The LIG patterns are rinsed with deionized water and ethanol, followed by drying. Applying Ag nanoparticles (Ag NPs) ink (AJ-191, Novacentrix) on the contact pads and drying at 80 °C (Fig. S6d) lower the contact resistance and ensure a good connection between the contact pads and copper ribbons through Ag epoxy adhesives (Fig. S6e).

3.4. Sensing performance characterizations

The cross-interference of different gas molecules in the mixture for practical applications facilitates the development of a gas sensor array with different sensing materials responding to different gas molecules and high selectivity in each sensing material. As a statistical method, the principal component analysis can also be used for the gas sensor array to identify the gas species [52]. To showcase the characteristic signature of

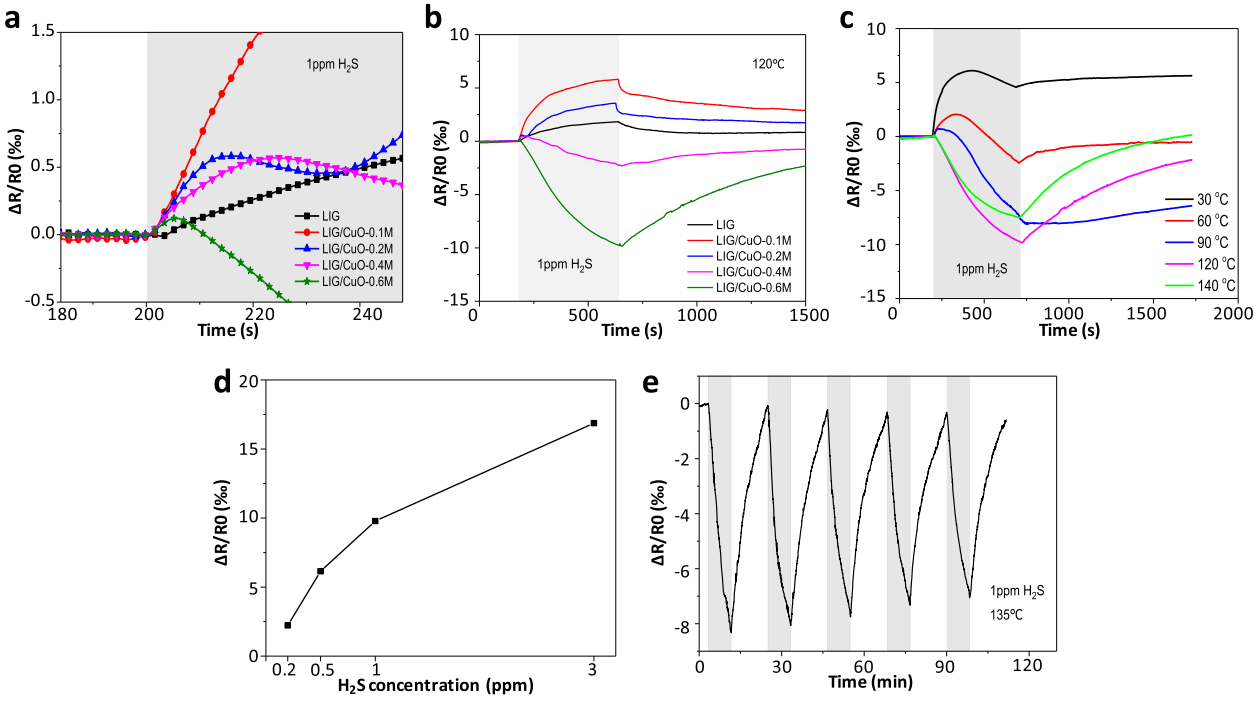

Fig. 5. The gas-sensing performance of the LIG/CuO composite to H_2S. (a) Initial responses and (b) full response/recovery process of the gas sensor based on the LIG/CuO composite with precursor solutions of various concentrations to 1 ppm H_2S at 120 °C. (c) The effect of operating temperature on the response of LIG/CuO-0.6 M to 1 ppm H_2S. (d) The sensitivity of LIG/CuO-0.6 M to various H_2S concentrations at 120 °C. (e) The cycling test of LIG/CuO-0.6 M to 1 ppm H_2S at 135 °C (a higher temperature was used to shorten the response/recovery time for the rapid repeatability test).

the sensing material to specific gas species [53], the gas-sensitive nanomaterials of MoS_2, CuO, and Ag/ZnO are selected as representative examples in this study to target NO_2, H_2S, and TMA due to their reported selectivity [54–56]. By leveraging the Joule heating effect [57,58], the gas sensors are self-heated up to the working temperature to evaluate their sensing performance to the target gas of varying concentrations. The raised working temperature can enhance the response/recovery rate by facilitating the gas adsorption/desorption[59], and minimize the effect of humidity in the ambient environment [8]. The temperature (referring to the highest value at the center) (Fig. S7) in the non-uniformly self-heated LIG is maintained to be below 150 °C to avoid damage.

Compared with the bare LIG gas sensor (response of 1.5 ‰ to 1 ppm NO_2 at 120 °C), the LIG/MoS_2 shows a significantly higher response

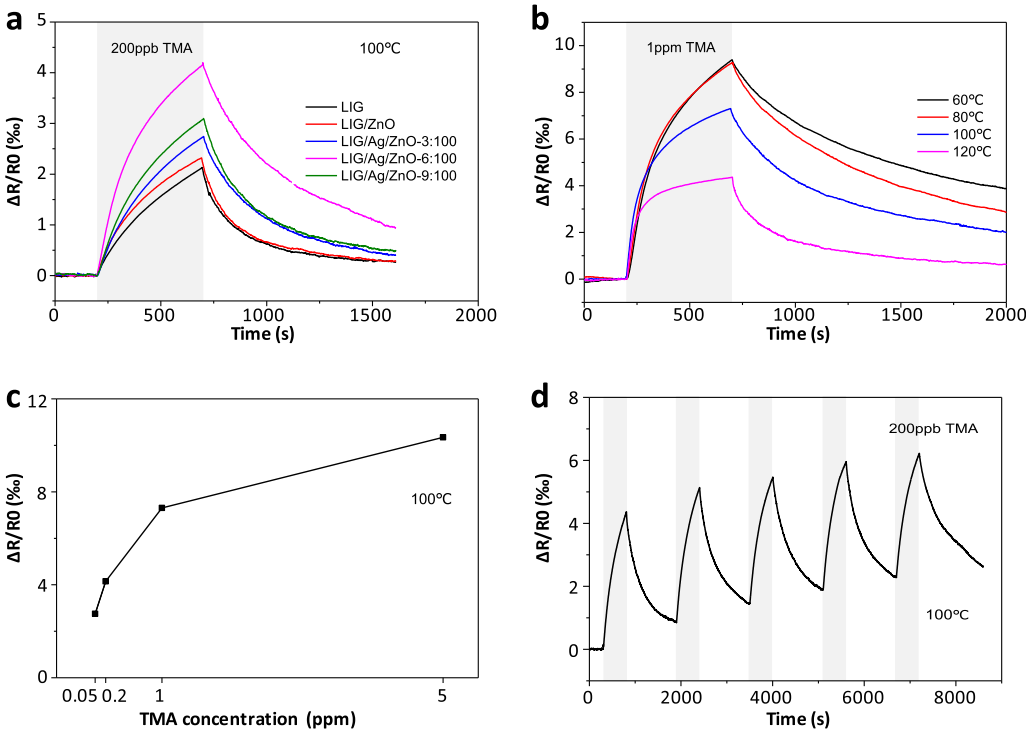

Fig. 6. The gas-sensing performance of LIG/ZnO and LIG/Ag/ZnO to TMA. (a) The response/recovery process of LIG/ZnO and LIG/Ag/ZnO gas sensors to 200 ppb TMA at 100 °C. (b) The effect of operating temperature on the response of LIG/Ag/ZnO-6:100 to 1 ppm TMA. (c) The sensitivity of LIG/Ag/ZnO-6:100 to various TMA concentrations at 100 °C. (d) The cycling test of LIG/Ag/ZnO-6:100 to 1 ppm TMA at 100 °C. Drifting of the sensor signal results from the incomplete recovery in rapid testing.

(Fig. 4a). The improved response is possibly attributed to the formation of the heterojunction between LIG and MoS_2 [8]. Due to the small amount and weak conductivity of doped *N*-type MoS_2 in the intrinsic P-type LIG, the LIG/MoS_2 composite has an overall P-type semiconductor characteristic. When exposed to oxidizing gas NO_2, the hole concentration on the material surface increases due to continuous electron transfer from LIG and MoS_2 to the adsorbed NO_2, which increases the conductivity and decreases the resistance. The combination of electrons and holes at the LIG/MoS_2 interface forms a charge depletion region to give a higher initial resistance. Although both the hole accumulation region on the LIG side and the charge depletion region on the MoS_2 side extend upon exposure to NO_2, the increase of holes has a larger impact to result in the decreased resistance as with the bare LIG sensor [60]. Additionally, the sensor fabricated with the precursor solution MoS_2-6:1 exhibits the highest response to NO_2 (>12 ‰ after 400 s exposure to NO_2) possibly due to the largest amount of the generated MOS_2.

The choice of the working temperature at 120 °C is justified by comparing the response of LIG/MoS_2-6:1 to 1 ppm NO_2 at different operating temperatures (Fig. 4b). Although the response gradually increases as the temperature is increased from 60 to 110 °C, further increasing the temperature to 120 °C does not give an increased response (despite the improved recovery of 91 % within 800 s in the air). The response of LIG/MoS_2-6:1 also rapidly increases from 2.3 to 12.2 ‰ as the NO_2 concentration increases from 0.1 to 1 ppm at 120 °C (Fig. 4c). However, a continued increase in the concentration from 1 to 10 ppm only gives a slow response increase from 12.2 to 17.6 ‰, possibly due to the saturation of NO_2 absorption at higher concentrations. Different from the IDE-based gas sensors, the LIG-based gas sensor eliminates the contact resistance between IDE and sensitive materials as LIG itself is used for both the electrode and sensitive material. Furthermore, the LIG composite with in situ synthesized MoS_2 can enhance both the physical and chemical interaction between MoS_2 and LIG when compared with dispensing MoS_2 on LIG. As a result, low noise and a high signal-to-noise ratio (SNR) can be obtained to result in increased sensitivity of 12.2 ‰ to 1 ppm NO_2 compared with that of 6.6 ‰ from dispensing hydrothermal-synthesized MoS_2 [6]. For example, the average noise (calculated from the standard deviation of 180 consecutive resistance values recorded before NO_2 exposure) of LIG/MoS_2-6:1 in the five tests is only 0.016 ‰ (Fig. S8). Although LIG/MoS_2-6:1 only has a response of 2.67 ‰ to 100 ppb NO_2, it showcases an SNR of 166.9 due to the extremely low noise level. According to the theoretical equation to calculate the Limit of Detection (LOD) for a linear sensor: LOD = 3 × noise/slope, the LOD is obtained as 2.7 ppb by using the slope from the linear fitting of the measurements between 100 and 300 ppb. Since the calibration curve of LIG/MoS_2-6:1 exhibits a much larger slope in the lower NO_2 concentration ranges, the actual LOD is postulated to be much lower than the above estimate. Good repeatability is also observed in the LIG/MoS_2-6:1 sensor during the cycling test (between 1 ppm NO_2 for 400 s and air for 800 s at 120 °C) (Fig. 4d). The slight baseline shift comes from the short recovery time for rapid testing, which leads to incomplete recovery. The sensors only exhibit a slight decrease in the response after three months, demonstrating good stability over time (Fig. S9).

The investigation of the LIG/CuO composite to H_2S (1 ppm at 120 °C) reveals two fundamental yet competing mechanisms (Fig. 5a). The bare P-type LIG absorbs oxygen in the air and forms the hole accumulation layer. When exposing the bare LIG sensor to reducing gas H_2S, oxygen ions on the LIG surface oxidize H_2S to release free electrons to the LIG for reduced carrier concentration and increased resistance. In the LIG/CuO composite, a homotypic heterojunction forms between LIG and CuO due to the different work functions of the two, with a hole accumulation layer formed on the surface of CuO as electrons flow from CuO to LIG [61]. The adsorption of oxygen in the air increases the thickness of the hole accumulation layer. Exposing the LIG/CuO composite to H_2S results in 1) the charge transfer between H_2S and LIG/CuO, and 2) the chemical reaction between H_2S and CuO. These two competing mechanisms lead to a two-stage response. The surface adsorbed oxygen on LIG and CuO first interacts with H_2S to withdraw electrons to reduce the thickness of the hole accumulation layer. Therefore, the resistance of the LIG/CuO composite is observed to increase to different degrees at the beginning. As the H_2S molecules start to react with CuO to form metallic conductor CuS in the second stage, the reduced resistance from the generated CuS would compete with the increased resistance through charge transfer between H_2S and LIG/CuO [62] (Fig. 5b). Because the amount of generated CuS is proportional to the concentration of the $Cu(NO_3)_2$ precursor solution, the LIG/CuO-0.1 M with the least amount of CuO shows a negligible effect of resistance reduction from CuS. The slightly higher amount of CuO in LIG/CuO-0.2 M forms CuS to reduce the resistance for a short period of time. The dominant role of LIG in the composite still allows the resistance to continue to increase as the hole accumulation layer decreases. However, the generated CuS from the relatively higher CuO content in LIG/CuO-0.4 M and LIG/CuO-0.6 M gradually dominates to result in the overall decrease in the sensor resistance. The largest resistance decrease in LIG/CuO-0.6 M reaches 9.8 ‰ with an SNR of 239 after 500 s exposure to H_2S.

The first increased and then decreased sensor resistance response that corresponds to the two competing mechanisms is observed when LIG/CuO-0.6 M is operated at 30, 60, and 90 °C (Fig. 5c). The more intense reaction between CuO and H_2S to form CuS at further increased temperatures to 120 and 140 °C dominates over the charge transfer between H_2S and sensing material resulting in the decreased resistance. Compared with that operated at 120 °C, the sensor at 140 °C shows a smaller response due to an enhanced inverse reaction that converts CuS back into CuO at a higher temperature. However, it is worth noting that the significantly improved recovery allows the sensor to fully recover within 800 s in air at 140 °C.

The response magnitude of LIG/CuO-0.6 M increases as the concentration of H_2S increases from 0.2 to 3 ppm at 120 °C (Fig. 5d and S10). Although the dominant mechanism from CuS usually occurs for a high H_2S concentration (>100 ppm) [63], the successful sensing of H_2S at ppb level through the chemical reaction is demonstrated in this study, possibly due to the highly porous structure of the LIG/CuO composite as in the flower-like nanostructure CuO [64]. The LOD is calculated to be 9.8 ppb by using the slope obtained from the linear fitting of the data between 200 and 500 ppb. The LIG/CuO-0.6 M sensor also shows very good repeatability in the cycling test (repeated exposure to 1 ppm H_2S and air) even at 135 °C (Fig. 5e).

The response (2.3 ‰) of LIG/ZnO is slightly higher than that (2.1 ‰) of the bare LIG to 200 ppb TMA at 100 °C (Fig. 6a), which is attributed to the enhanced charge transfer and formation of the heterojunction between p-type LIG and *n*-type ZnO [65–67]. Because of the overflow effect from the Ag catalytic property to create additional active sites on the sensor surface for more TMA absorption [68], Ag doping significantly improves the sensor response, with the largest response of 4.2 ‰ from LIG/Ag/ZnO-6:100. Although LIG/Ag/ZnO-9:100 has more Ag loading than LIG/Ag/ZnO-6:100, the sensor response is smaller, likely due to the imbalanced oxygen distribution on the sensing material surface [69].

The response of LIG/Ag/ZnO-6:100 to 1 ppm TMA increases as the temperature drops from 120 to 80 °C, which further saturates at 60 °C (Fig. 6b). Meanwhile, the decreased temperature deteriorates the recovery performance. Therefore, the temperature of 100 °C is chosen for the balanced response and recovery in the following studies unless specifies otherwise. The response of LIG/Ag/ZnO-6:100 to TMA also first rapidly increases with the concentration from 50 ppb to 1 ppm, and then slowly increases with the increasing concentration from 1 to 5 ppm, partly due to the saturation of TMA absorption (Fig. 6c and S11). At a low concentration of 50 ppb, LIG/Ag/ZnO-6:100 still exhibits a large SNR of 157 due to the extremely low noise level (0.0175 ‰) despite the small response of 2.75 ‰. By using the slope from the linear fitting of the data between 50 and 200 ppb, the estimated LOD is calculated to be 5.6 ppb, with the actual LOD expected to be much lower. Good repeatability is also observed in the LIG/Ag/ZnO-6:100 sensor during the cycling test (between 200 ppb TMA for 400 s and air for 1100 s at 100 °C) (Fig. 6d).

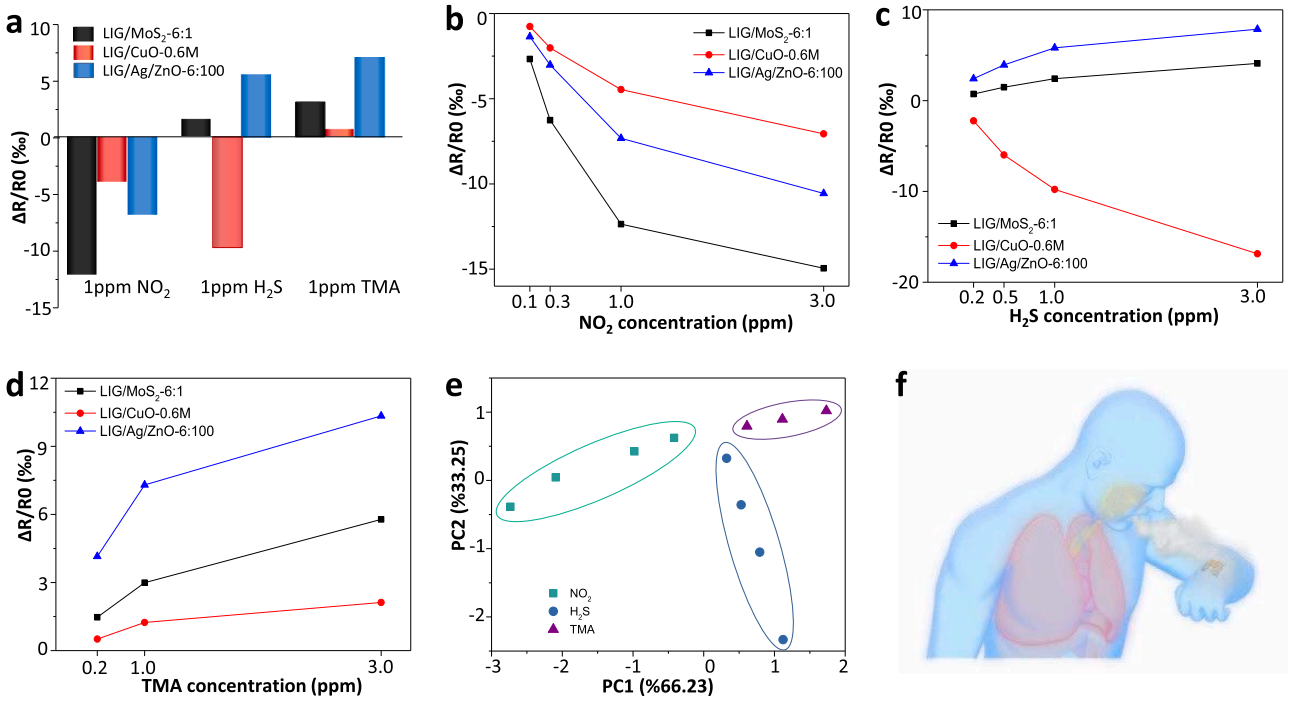

Fig. 7. The gas-sensing performance and application of the sensor array. (a) The response patterns of the sensor array to 1 ppm NO_2, H_2S, and TMA. The responses and corresponding fitting lines of each sensor within the array to various concentrations of (b) NO_2, (c) H_2S, and (d) TMA. (e) PCA results of the array responses to the three gases. (f) Exhaled breath analysis is one of the future application of the sensor array.

The slight baseline shift can be avoided by either increasing the working temperature or the recovery time during the test.

Finally, the notable selectivity of LIG/MoS_2-6:1 (at 120 °C), LIG/CuO-0.6 M (at 120 °C), and LIG/Ag/ZnO-6:100 (at 100 °C) (Fig. S12) provides the route to integrate them into a single sensor array to potentially deconvolute multiple gas species in the mixture. The humidity effect on the sensor performance can be further reduced by exploring a breathable hydrophobic coating [70]. The proof-of-concept demonstration focused on sensing device for the detection of NO_X, H_2S, and TMA, which are not only common industrial toxicants and air pollutants in the environment, but also biomarkers in human exhaled breath for noninvasive diagnosis of respiratory inflammation and diseases in the lung, kidney, and liver [71,72]. In the proof-of-concept demonstration, the gas sensor array is sequentially exposed to three different gases with a concentration of 1 ppm. The exposure to NO_2 results in the highest response (12.2 ‰) from LIG/MoS_2-6:1, followed by 7.3 ‰ from LIG/Ag/ZnO-6:100 and 4.5 ‰ from LIG/CuO-0.6 M (Fig. S13a). When exposed to H_2S, the resistance of LIG/MoS_2-6:1 and LIG/Ag/ZnO-6:100 increases by 2.5 ‰ and 5.9 ‰, respectively, whereas that of LIG/CuO-0.6 M decreases by 9.8 ‰ (Fig. S13b). The detection of TMA is captured by the highest response of 7.7 ‰ from LIG/Ag/ZnO-6:100, followed by 3.0 ‰ from LIG/MoS_2-6:1 and 1.3 ‰ from LIG/CuO-0.6 M (Fig. S13c). Each gas produced a unique response pattern across the sensor array by which precise identification of cross-sensitive gases is possible (Fig. 7a). When exposed to more concentrations of the three gases, the response pattern of the sensor array to each gas (the direction of the response of the three sensors and the amplitude contrast among them) is generally maintained (Fig. 7b-d). Principal component analysis (PCA) study is performed on these responses to reduce the dimensions of the data, and the results show clear separations among the gas clusters (Fig. 7e). When further combined machine learning methods [73,74], the reported sensor array can deconvolute multiple gas species in the mixture and pave the way for wearable ambient gases detection or exhaled breath analysis (Fig. 7f).

4. Conclusion

In summary, this work reported a rapid and lost-cost method to simultaneously pattern, synthesize, and integrate varying semiconducting materials (e.g., MoS_2, CuO, Ag/ZnO, and In_2O_3/Cr_2O_3) on LIG to form functional LIG composites via laser scribing of LIG with different precursor solutions. Compared with traditional methods to fabricate composite nanomaterials, the demonstrated method easily created gas sensors based on the LIG composites within a few minutes in the ambient environment without the use of surfactant. Different from the pure LIG, the gas sensor based on the LIG composite nanomaterials exhibited programmable selectivity, including LIG/MoS_2 to NO_2, LIG/CuO to H_2S, and LIG/Ag/ZnO to TMA. The in situ growth of varying functional nanomaterials eliminated the contact resistance in the traditional IDE-based sensors to give low noise and high SNR, leading to (sub) ppb level detection of NO_2, H_2S, and TMA. More importantly, the rich library of LIG composites based on the integration of LIG with varying semiconducting materials could potentially provide a high-density sensor array to deconvolute multiple gas species in the mixture. Additionally, the in situ synthesis of graphene foam composites and the rich material library can be applied to optimize the design of LIG-based materials for biochemical sensing, physical physiological sensing, electrocatalysis, and energy storage.

Declaration of Competing Interest

The authors declare that they have no known competing financial interests or personal relationships that could have appeared to influence the work reported in this paper.

Data availability

Data will be made available on request.

Acknowledgments

is research is supported by NIH (Award Nos. R21EB030140, U01DA056242, and R61HL154215), NSF (Grant Nos. ECCS-1933072 and CMMI-2046819), Sloan Research Fellowship (Grant No. FG-2020-12707), and Penn State University. One or more provisional patents are being filed on this work.

Appendix A. Supplementary data

Supplementary data to this article can be found online at https://doi.org/10.1016/j.cej.2022.140956.

References

[1] J. Aponte-Luis, J.A. Gómez-Galán, F. Gómez-Bravo, M. Sánchez-Raya, J. Alcina-Espigado, P.M. Teixido-Rovira, An efficient wireless sensor network for industrial monitoring and control, Sensors 18 (1) (2018) 182, https://doi.org/10.3390/s18010182.

[2] Z. Song, W. Ye, Z. Chen, Z. Chen, M. Li, W. Tang, C. Wang, Z. Wan, S. Poddar, X. Wen, X. Pan, Y. Lin, Q. Zhou, Z. Fan, Wireless self-powered high-performance integrated nanostructured-gas-sensor network for future smart homes, ACS Nano 15 (4) (2021) 7659–7667.

[3] X. Zheng, H. Cheng, Flexible and stretchable metal oxide gas sensors for healthcare, Sci. China Technol. Sci. 62 (2) (2019) 209–223, https://doi.org/10.1007/s11431-018-9397-5.

[4] J. Lin, Z. Peng, Y. Liu, F. Ruiz-Zepeda, R. Ye, E.L. Samuel, M.J. Yacaman, B. I. Yakobson, J.M. Tour, Laser-induced porous graphene films from commercial polymers, Nat. Commun. 5 (1) (2014) 1–8, https://doi.org/10.1038/ncomms6714.

[5] L.i. Yang, H. Ji, C. Meng, Y. Li, G. Zheng, X. Chen, G. Niu, J. Yan, Y.e. Xue, S. Guo, H. Cheng, Intrinsically Breathable and Flexible NO2 Gas Sensors Produced by Laser Direct Writing of Self-Assembled Block Copolymers, ACS Appl. Mater. Interfaces 14 (15) (2022) 17818–17825.

[6] L. Yang, N. Yi, J. Zhu, Z. Cheng, X. Yin, X. Zhang, H. Zhu, H. Cheng, Novel gas sensing platform based on a stretchable laser-induced graphene pattern with self-heating capabilities, J. Mater. Chem. A 8 (14) (2020) 6487–6500, https://doi.org/10.1039/C9TA07855J.

[7] M.G. Stanford, K. Yang, Y. Chyan, C. Kittrell, J.M. Tour, Laser-induced graphene for flexible and embeddable gas sensors, ACS Nano 13 (3) (2019) 3474–3482, https://doi.org/10.1021/acsnano.8b09622.

[8] N. Yi, Z. Cheng, H. Li, L. Yang, J. Zhu, X. Zheng, Y. Chen, Z. Liu, H. Zhu, H. Cheng, Stretchable, ultrasensitive, and low-temperature NO2 sensors based on MoS2@rGO nanocomposites, Mater. Today Phys. 15 (2020), 100265, https://doi.org/10.1016/j.mtphys.2020.100265.

[9] J. Zhu, M. Cho, Y. Li, I. Cho, J.-H. Suh, D.D. Orbe, Y. Jeong, T.-L. Ren, I. Park, Biomimetic turbinate-like artificial nose for hydrogen detection based on 3D porous laser-induced graphene, ACS Appl. Mater. Interfaces 11 (27) (2019) 24386–24394, https://doi.org/10.1021/acsami.9b04495.

[10] M. Dosi, I. Lau, Y. Zhuang, D.S. Simakov, M.W. Fowler, M.A. Pope, Ultrasensitive electrochemical methane sensors based on solid polymer electrolyte-infused laser-induced graphene, ACS Appl. Mater. Interfaces 11 (6) (2019) 6166–6173, https://doi.org/10.1021/acsami.8b22310.

[11] C. Wang, L. Yin, L. Zhang, D. Xiang, R. Gao, Metal oxide gas sensors: sensitivity and influencing factors, Sensors 10 (3) (2010) 2088–2106, https://doi.org/10.3390/s100302088.

[12] S. Yang, C. Jiang, S.-H. Wei, Gas sensing in 2D materials, Appl. Phys. Rev. 4 (2) (2017), 021304, https://doi.org/10.1063/1.4983310.

[13] S. Guo, D. Yang, S. Zhang, Q. Dong, B. Li, N. Tran, Z. Li, Y. Xiong, M.E. Zaghloul, Development of a cloud-based epidermal MoSe2 device for hazardous gas sensing, Adv. Funct. Mater. 29 (18) (2019) 1900138, https://doi.org/10.1002/adfm.201900138.

[14] I. Karaduman, E. Er, H. Çelikkan, N. Erk, S. Acar, Room-temperature ammonia gas sensor based on reduced graphene oxide nanocomposites decorated by Ag, Au and Pt nanoparticles, J. Alloy. Compd. 722 (2017) 569–578, https://doi.org/10.1016/j.jallcom. 2017.06.152.

[15] W.-H. Tao, C.-H. Tsai, H2S sensing properties of noble metal doped WO3 thin film sensor fabricated by micromachining, Sens. Actuators B 81 (2–3) (2002) 237–247, https://doi.org/10.1016/S0925-4005(01)00958-3.

[16] T. Mochida, K. Kikuchi, T. Kondo, H. Ueno, Y. Matsuura, Highly sensitive and selective H2S gas sensor from rf sputtered SnO2 thin film, Sens. Actuators B 25 (1–3) (1995) 433–437, https://doi.org/10.1016/0925-4005(95)85098-8.

[17] P.-C. Chou, H.-I. Chen, I.-P. Liu, C.-C. Chen, J.-K. Liou, K.-S. Hsu, W.-C. Liu, On the ammonia gas sensing performance of a RF sputtered NiO thin-film sensor, IEEE Sens. J. 15 (7) (2015) 3711–3715, https://doi.org/10.1109/JSEN.2015.2391286.

[18] D. Punetha, S.K. Pandey, CO gas sensor based on E-beam evaporated ZnO, MgZnO, and CdZnO thin films: A comparative study, IEEE Sens. J. 19 (7) (2018) 2450–2457, https://doi.org/10.1109/JSEN.2018.2890007.

[19] Y. Hu, O. Tan, W. Cao, W. Zhu, A low temperature nano-structured SrTiO3 thick film oxygen gas sensor, Ceram. Int. 30(7) (2004) 1819-1822. doi: 10.1016/ j. ceramint .2003.12.068 doi: 10.1016/j.ceramint.2003.12.068.

[20] E. Dai, S. Wu, Y. Ye, Y. Cai, J. Liu, C. Liang, Highly dispersed Au nanoparticles decorated WO3 nanoplatelets: Laser-assisted synthesis and superior performance for detecting ethanol vapor, J. Colloid Interface Sci. 514 (2018) 165–171, https://doi.org/10.1016/j.jcis.2017.11.081.

[21] W. Li, J. Lin, X. Wang, J. Jiang, S. Guo, G. Zheng, Electrospray deposition of ZnO thin films and its application to gas sensors, Micromachines 9 (2) (2018) 66, https://doi.org/10.3390/mi9020066.

[22] R. Artzi-Gerlitz, K.D. Benkstein, D.L. Lahr, J.L. Hertz, C.B. Montgomery, J. E. Bonevich, S. Semancik, M.J. Tarlov, Fabrication and gas sensing performance of parallel assemblies of metal oxide nanotubes supported by porous aluminum oxide membranes, Sens. Actuators B 136 (1) (2009) 257–264, https://doi.org/10.1016/j.snb.2008.10.056.

[23] P. Sun, W. Wang, Y. Liu, Y. Sun, J. Ma, G. Lu, Hydrothermal synthesis of 3D urchin-like α-Fe2O3 nanostructure for gas sensor, Sens. Actuators B 173 (2012) 52–57, https://doi.org/10.1016/j.snb.2012.05.057.

[24] R.L. Fomekong, H.T. Kamta, J.N. Lambi, D. Lahem, P. Eloy, M. Debliquy, A. Delcorte, A sub-ppm level formaldehyde gas sensor based on Zn-doped NiO prepared by a co-precipitation route, J. Alloy. Compd. 731 (2018) 1188–1196, https://doi.org/10.1016/j.jallcom.2017.10.089.

[25] T. Xu, Y. Pei, Y. Liu, D. Wu, Z. Shi, J. Xu, Y. Tian, X. Li, High-response NO2 resistive gas sensor based on bilayer MoS2 grown by a new two-step chemical vapor deposition method, J. Alloy. Compd. 725 (2017) 253–259, https://doi.org/10.1016/j.jallcom.2017.06.105.

[26] S.K. Lim, S.H. Hong, S.-H. Hwang, W.M. Choi, S. Kim, H. Park, M.G. Jeong, Synthesis of Al-doped ZnO nanorods via microemulsion method and their application as a CO gas sensor, J. Mater. Sci. Technol. 31 (6) (2015) 639–644, https://doi.org/10.1016/j.jmst.2014.12.004.

[27] S.-X. Liang, L.-C. Zhang, S. Reichenberger, S. Barcikowski, Design and perspective of amorphous metal nanoparticles from laser synthesis and processing, PCCP 23 (19) (2021) 11121–11154, https://doi.org/10.1039/D1CP00701G.

[28] B. Pandey, A. Shahi, J. Shah, R. Kotnala, R. Gopal, Optical and magnetic properties of Fe2O3 nanoparticles synthesized by laser ablation/fragmentation technique in different liquid media, Appl. Surf. Sci. 289 (2014) 462–471, https://doi.org/10.1016/j.apsusc. 2013.11.009.

[29] M. Zhilnikova, E. Barmina, I. Pavlov, A. Vasiliev, G. Shafeev, Laser fragmentation of Ag2O micropowder in water, J. Phys. Chem. Solid 160 (2022), 110356, https://doi.org/10.1016/j.jpcs.2021.110356.

[30] M. Yu, F. Waag, C.K. Chan, C. Weidenthaler, S. Barcikowski, H. Tüysüz, Laser fragmentation-induced defect-rich cobalt oxide nanoparticles for electrochemical oxygen evolution reaction, ChemSusChem 13 (3) (2020) 520–528, https://doi.org/10.1002/cssc.201903186.

[31] R. Torres-Mendieta, O. Havelka, M. Urbánek, M. Cvek, S. Wacławek, V.V.T. Padil, D. Jašíková, M. Kotek, M. Černík, Laser-assisted synthesis of Fe-Cu oxide nanocrystals, Appl. Surf. Sci. 469 (2019) 1007–1015, https://doi.org/10.1016/j.apsusc.2018.11.058.

[32] S.S. Naik, S.J. Lee, S. Yeon, Y. Yu, M.Y. Choi, Pulsed laser-assisted synthesis of metal and nonmetal-codoped ZnO for efficient photocatalytic degradation of Rhodamine B under solar light irradiation, Chemosphere 274 (2021), 129782, https://doi.org/10.1016/j.chemosphere.2021.129782.

[33] M. Censabella, V. Iacono, A. Scandurra, K. Moulaee, G. Neri, F. Ruffino, S. Mirabella, Low temperature detection of nitric oxide by CuO nanoparticles synthesized by pulsed laser ablation, Sens. Actuators B 358 (2022), 131489, https://doi.org/10.1016/j.snb.2022. 131489.

[34] V. Amendola, D. Amans, Y. Ishikawa, N. Koshizaki, S. Scirè, G. Compagnini, S. Reichenberger, S. Barcikowski, Room-temperature laser synthesis in liquid of oxide, metal-oxide core-shells, and doped oxide nanoparticles, Chemistry–A, European Journal 26 (42) (2020) 9206–9242, https://doi.org/10.1002/chem.202000686.

[35] W. Yan, W. Yan, T. Chen, J. Xu, Q. Tian, D. Ho, Size-tunable flowerlike MoS2 nanospheres combined with laser-induced graphene electrodes for NO2 sensing, ACS Appl. Nano Mater. 3 (3) (2020) 2545–2553, https://doi.org/10.1021/acsanm.9b02614.

[36] F. Clerici, M. Fontana, S. Bianco, M. Serrapede, F. Perrucci, S. Ferrero, E. Tresso, A. Lamberti, In situ MoS2 decoration of laser-induced graphene as flexible supercapacitor electrodes, ACS Appl. Mater. Interfaces 8 (16) (2016) 10459–10465, https://doi.org/10.1021/acsami.6b00808.

[37] R. Ye, Z. Peng, T. Wang, Y. Xu, J. Zhang, Y. Li, L.G. Nilewski, J. Lin, J.M. Tour, In situ formation of metal oxide nanocrystals embedded in laser-induced graphene, ACS Nano 9 (9) (2015) 9244–9251, https://doi.org/10.1021/acsnano.5b04138.

[38] H. Yoon, J. Nah, H. Kim, S. Ko, M. Sharifuzzaman, S.C. Barman, X. Xuan, J. Kim, J. Y. Park, A chemically modified laser-induced porous graphene based flexible and ultrasensitive electrochemical biosensor for sweat glucose detection, Sens. Actuators B 311 (2020), 127866, https://doi.org/10.1016/j.snb.2020.127866.

[39] G. Zhao, Y. Ling, Y. Su, Z. Chen, C.J. Mathai, O. Emeje, A. Brown, D.R. Alla, J. Huang, C. Kim, Q. Chen, X. He, D. Stalla, Y. Xu, Z. Chen, P.-Y. Chen, S. Gangopadhyay, J. Xie, Z. Yan, Laser-scribed conductive, photoactive transition metal oxide on soft elastomers for Janus on-skin electronics and soft actuators, Sci. Adv. 8 (25) (2022), https://doi.org/10.1126/sciadv.abp9734.

[40] Y. Li, D.X. Luong, J. Zhang, Y.R. Tarkunde, C. Kittrell, F. Sargunaraj, Y. Ji, C. J. Arnusch, J.M. Tour, Laser-Induced Graphene in Controlled Atmospheres: From Superhydrophilic to Superhydrophobic Surfaces, Adv. Mater. 29 (27) (2017) 1700496.

[41] Z. Li, R. Fan, Z. Hu, W. Li, H. Zhou, S. Kang, Y. Zhang, H. Zhang, G. Wang, Ethanol introduced synthesis of ultrastable 1T-MoS2 for removal of Cr (VI), J. Hazard. Mater. 394 (2020), 122525, https://doi.org/10.1016/j.jhazmat.2020.122525.

[42] A. Chhetry, M. Sharifuzzaman, H. Yoon, S. Sharma, X. Xuan, J.Y. Park, MoS2-decorated laser-induced graphene for a highly sensitive, hysteresis-free, and

reliable piezoresistive strain sensor, ACS Appl. Mater. Interfaces 11 (25) (2019) 22531–22542, https://doi.org/10.1021/acsami.9b04915.
[43] L. Kumari, Y.-R. Ma, C.-C. Tsai, Y.-W. Lin, S.Y. Wu, K.-W. Cheng, Y. Liou, X-ray diffraction and Raman scattering studies on large-area array and nanobranched structure of 1D MoO2 nanorods, Nanotechnology 18 (11) (2007), 115717, https://doi.org/10.1088/0957-4484/18/11/115717.
[44] C. Liu, S. Luo, H. Huang, Y. Zhai, Z. Wang, Direct growth of MoO2/reduced graphene oxide hollow sphere composites as advanced anode materials for potassium-ion batteries, ChemSusChem 12 (4) (2019) 873–880, https://doi.org/10.1002/cssc.201802494.
[45] M. Balık, V. Bulut, I.Y. Erdogan, Optical, structural and phase transition properties of Cu2O, CuO and Cu2O/CuO: Their photoelectrochemical sensor applications, Int. J. Hydrogen Energy 44 (34) (2019) 18744–18755, https://doi.org/10.1016/j.ijhydene. 2018.08.159.
[46] G. Durai, P. Kuppusami, K. Viswanathan, Investigation on microstructure and improved supercapacitive performance of Mn doped CuO thin films prepared by reactive radio frequency magnetron sputtering, J. Mater. Sci. Mater. Electron. 29 (3) (2018) 2051–2058, https://doi.org/10.1007/s10854-017-8118-5.
[47] Q. Huang, J. Li, X. Bi, The improvement of hole transport property and optical band gap for amorphous Cu2O films, J. Alloy. Compd. 647 (2015) 585–589, https://doi.org/10.1016/j.jallcom.2015.06.147.
[48] S. Deng, V. Tjoa, H.M. Fan, H.R. Tan, D.C. Sayle, M. Olivo, S. Mhaisalkar, J. Wei, C. H. Sow, Reduced graphene oxide conjugated Cu2O nanowire mesocrystals for high-performance NO2 gas sensor, J. Am. Chem. Soc. 134 (10) (2012) 4905–4917, https://doi.org/10.1021/ja211683m.
[49] L.-L. Yang, J.-H. Yang, D.-D. Wang, Y.-J. Zhang, Y.-X. Wang, H.-L. Liu, H.-G. Fan, J.-H. Lang, Photoluminescence and Raman analysis of ZnO nanowires deposited on Si (1 0 0) via vapor–liquid–solid process, Physica E 40 (4) (2008) 920–923, https://doi.org/10.1016/j.physe.2007.11.025.
[50] J. Wang, G. Huang, X. Zhong, L. Sun, Y. Zhou, E. Liu, Raman scattering and high temperature ferromagnetism of Mn-doped ZnO nanoparticles, Appl. Phys. Lett. 88 (25) (2006), 252502, https://doi.org/10.1063/1.2208564.
[51] H. Bian, S. Ma, F. Li, H. Zhu, Influence of ZnO buffer layer on microstructure and Raman scattering of ZnO: Ag film on Si substrate, Superlattice. Microst. 58 (2013) 171–177, https://doi.org/10.1016/j.spmi.2013.03.017.
[52] T.I.T. Akamatsu, A. Tsuruta, W. Shin, Selective detection of target volatile organic compounds in contaminated humid air using a sensor array with principal component analysis, Sensors 17 (7) (2017) 1662, https://doi.org/10.3390/s17071662.
[53] A. Star, V. Joshi, S. Skarupo, D. Thomas, J.-C.-P. Gabriel, Gas sensor array based on metal-decorated carbon nanotubes, J. Phys. Chem. B 110 (42) (2006) 21014–21020, https://doi.org/10.1021/jp064371z.
[54] R. Kumar, P.K. Kulriya, M. Mishra, F. Singh, G. Gupta, M. Kumar, Highly selective and reversible NO2 gas sensor using vertically aligned MoS2 flake networks, Nanotechnology 29 (46) (2018) 464001.
[55] Y. Li, L. Jing, Z. Tao, J. Chen, CuO particles and plates: Synthesis and gas-sensor application, Mater. Res. Bull. 43 (8–9) (2008) 2380–2385, https://doi.org/10.1016/j.materresbull.2007.07.045.
[56] F. Meng, H. Zheng, Y. Sun, M. Li, J. Liu, Trimethylamine sensors based on Au-modified hierarchical porous single-crystalline ZnO nanosheets, Sensors 17 (7) (2017) 1478, https://doi.org/10.3390/s17071478.
[57] D. Wu, Q. Peng, S. Wu, G. Wang, L. Deng, H. Tai, L. Wang, Y. Yang, L. Dong, Y. Zhao, A Simple Graphene NH3 Gas Sensor via Laser Direct Writing, Sensors 18 (12) (2018) 4405, https://doi.org/10.3390/s18124405.
[58] M.R. Bobinger, F.J. Romero, A. Salinas-Castillo, M. Becherer, P. Lugli, D. P. Morales, N. Rodríguez, A. Rivadeneyra, Flexible and robust laser-induced graphene heaters photothermally scribed on bare polyimide substrates, Carbon 144 (2019) 116–126, https://doi.org/10.1016/j.carbon.2018.12.010.
[59] H. Long, A. Harley-Trochimczyk, T. Pham, Z. Tang, T. Shi, A. Zettl, C. Carraro, M. A. Worsley, R. Maboudian, High surface area MoS2/graphene hybrid aerogel for ultrasensitive NO2 detection, Adv. Funct. Mater. 26 (28) (2016) 5158–5165, https://doi.org/10.1002/adfm.201601562.
[60] Y. Zhou, G. Liu, X. Zhu, Y. Guo, Ultrasensitive NO2 gas sensing based on rGO/MoS2 nanocomposite film at low temperature, Sens. Actuators B 251 (2017) 280–290, https://doi.org/10.1016/j.snb.2017.05.060.
[61] J.-H. Kim, A. Mirzaei, Y. Zheng, J.-H. Lee, J.-Y. Kim, H.W. Kim, S.S. Kim, Enhancement of H2S sensing performance of p-CuO nanofibers by loading p-reduced graphene oxide nanosheets, Sens. Actuators B 281 (2019) 453–461, https://doi.org/10.1016/j.snb.2018.10.144.
[62] N. Ramgir, S.K. Ganapathi, M. Kaur, N. Datta, K. Muthe, D. Aswal, S. Gupta, J. Yakhmi, Sub-ppm H2S sensing at room temperature using CuO thin films, Sens. Actuators B 151 (1) (2010) 90–96, https://doi.org/10.1016/j.snb.2010.09.043.
[63] H. Kim, C. Jin, S. Park, S. Kim, C. Lee, H2S gas sensing properties of bare and Pd-functionalized CuO nanorods, Sens. Actuators B 161 (1) (2012) 594–599, https://doi.org/10.1016/j.snb.2011.11.006.
[64] Z. Li, J. Wang, N. Wang, S. Yan, W. Liu, Y.Q. Fu, Z. Wang, Hydrothermal synthesis of hierarchically flower-like CuO nanostructures with porous nanosheets for excellent H2S sensing, J. Alloy. Compd. 725 (2017) 1136–1143, https://doi.org/10.1016/j.jallcom. 2017.07.218.
[65] H.W. Kim, Y.J. Kwon, A. Mirzaei, S.Y. Kang, M.S. Choi, J.H. Bang, S.S. Kim, Synthesis of zinc oxide semiconductors-graphene nanocomposites by microwave irradiation for application to gas sensors, Sens. Actuators B 249 (2017) 590–601, https://doi.org/10.1016/j.snb.2017.03.149.
[66] H. Zhang, Y. Cen, Y. Du, S. Ruan, Enhanced acetone sensing characteristics of ZnO/graphene composites, Sensors 16 (11) (2016) 1876, https://doi.org/10.3390/s16111876.
[67] G. Singh, A. Choudhary, D. Haranath, A.G. Joshi, N. Singh, S. Singh, R. Pasricha, ZnO decorated luminescent graphene as a potential gas sensor at room temperature, Carbon 50 (2) (2012) 385–394, https://doi.org/10.1016/j.carbon.2011.08.050.
[68] A.I. Uddin, K.-W. Lee, G.-S. Chung, Acetylene gas sensing properties of an Ag-loaded hierarchical ZnO nanostructure-decorated reduced graphene oxide hybrid, Sens. Actuators B 216 (2015) 33–40, https://doi.org/10.1016/j.snb.2015.04.028.
[69] E. Wongrat, N. Hongsith, D. Wongratanaphisan, A. Gardchareon, S. Choopun, Control of depletion layer width via amount of AuNPs for sensor response enhancement in ZnO nanostructure sensor, Sens. Actuators B 171 (2012) 230–237, https://doi.org/10.1016/j.snb.2012.03.050.
[70] Y. Tan, B. Du, C. Liang, X. Guo, H. Zheng, P. Liu, X.i. Yang, S. Li, B.o. Jin, J. Sun, Improving Anti-Humidity Property of a SnO2Based Chemiresistive Hydrogen Sensor by a Breathable and Hydrophobic Fluoropolymer Coating, Langmuir 38 (45) (2022) 13833–13840.
[71] T. Chen, T. Liu, T. Li, H. Zhao, Q. Chen, Exhaled breath analysis in disease detection, Clin. Chim. Acta 515 (2021) 61–72, https://doi.org/10.1016/j.cca.2020.12.036.
[72] I.A. Hanouneh, N.N. Zein, F. Cikach, L. Dababneh, D. Grove, N. Alkhouri, R. Lopez, R.A. Dweik, The breathprints in patients with liver disease identify novel breath biomarkers in alcoholic hepatitis, Clin. Gastroenterol. Hepatol. 12 (3) (2014) 516–523, https://doi.org/10.1016/j.cgh.2013.08.048.
[73] V. Binson, M. Subramoniam, L. Mathew, Detection of COPD and Lung Cancer with electronic nose using ensemble learning methods, Clin. Chim. Acta 523 (2021) 231–238, https://doi.org/10.1016/j.cca.2021.10.005.
[74] N.J. Pineau, J.F. Kompalla, A.T. Güntner, S.E. Pratsinis, Orthogonal gas sensor arrays by chemoresistive material design, Microchim. Acta 185 (12) (2018) 1–9, https://doi.org/10.1007/s00604-018-3104-z.